RSC Advances

ROYAL SOCIETY OF CHEMISTRY

PAPER

View Article Online
View Journal | View Issue

Check for updates

Cite this: *RSC Adv.*, 2025, **15**, 7926

Tailoring alginate nanoparticles: influence of reverse micelle templates on structure, size, and encapsulation properties†

Fanny Melina Duque,[ab] R. Dario Falcone[ab] and N. Mariano Correa*[ab]

Received 6th December 2024
Accepted 9th March 2025

DOI: 10.1039/d4ra08616c

rsc.li/rsc-advances

In this work, alginate nanoparticles (ALG-NPs) were synthesized using reverse micelles (RMs) as nanoreactors to investigate how interfacial charge influences their structure, size, and encapsulation properties. Three types of RMs were employed: (i) anionic RMs formed by sodium bis(2-ethylhexyl)sulfosuccinate (AOT) in isopropyl myristate, (ii) cationic RMs formed by benzyl-hexadecyl-dimethylammonium chloride (BHDC) in toluene, and (iii) nonionic RMs formed by 2-[4-(2,4,4-trimethylpentan-2-yl)phenoxy]ethanol (TX-100) in cyclohexane. ALG-NPs were synthesized at varying water contents (W_0 = $[H_2O]/[surfactant]$) and resuspended in water at pH 6.5 for characterization. Dynamic light scattering revealed that nanoparticle size is highly dependent on the RM template. ALG-NPs synthesized in AOT RMs were the smallest, with their size increasing as W_0 increased, a trend also observed for TX-100 RMs. In contrast, the opposite behavior was observed in BHDC RMs, where nanoparticle size decreased with increasing W_0. This difference reflects the degree of crosslinking with Ca^{2+} ions as influenced by interfacial charge. Using *N*,*N*-dimethyl-6-propionyl-2-naphthylamine (PRODAN) and curcumin, we found that AOT-based ALG-NPs were the most compact and rigid, offering prolonged protection for curcumin against degradation under ambient conditions. This study underscores the potential of tailoring ALG-NPs through precise control of interfacial environments, offering new opportunities for applications in food technology, nutraceuticals, and biotechnology. By stabilizing bioactive compounds and enhancing bioavailability, these findings pave the way for innovative functional formulations.

1. Introduction

Organized systems are increasingly utilized as nanoreactors for synthesizing a diverse range of nanomaterials, offering a flexible and efficient alternative to conventional methods. Among these systems, reverse micelles (RMs) stand out as a prominent example. RMs form when specific surfactants dissolve in a non-polar organic solvent, driven by the amphiphilic nature of the surfactants. These molecules possess distinct polar and non-polar regions: the non-polar segment, typically a long hydrocarbon chain, aligns with the organic solvent, while the polar region, often composed of charged salts or polar functional groups, faces away from the non-polar medium.[1–5]

The properties of RMs depend critically on the choice of surfactant and non-polar solvent, enabling the study of various interfacial environments. For instance, the anionic surfactant sodium bis(2-ethylhexyl)sulfosuccinate (AOT) (Scheme 1) forms RMs in solvents such as the biocompatible isopropyl myristate (IPM), while the cationic surfactant benzyl-hexadecyl-dimethylammonium chloride (BHDC) (Scheme 1) forms RMs exclusively in aromatic solvents like toluene. Conversely, the non-ionic surfactant Triton X-100 (TX-100 in Scheme 1) creates RMs in cyclohexane.[6–9] These variations significantly influence the micelle interface and the organization of encapsulated water, quantified by the parameter W_0 = [water]/[surfactant].[10]

On the other hand, polymeric nanoparticles (NPs) have garnered significant attention across diverse scientific and technological fields.[11,12] These systems are designed to enhance therapeutic efficacy and bioavailability in applications such as drug and gene delivery, enabling controlled release and optimized distribution of active compounds.[13–16] In the food sector, polymeric NPs are employed to encapsulate nutrients and improve sensory properties like flavor and texture.[17–19] The production of these NPs can be achieved using a variety of materials, including polysaccharides, proteins, and synthetic polymers. Several synthesis methods are available, including desolvation, dialysis, ionic gelation, nanoprecipitation, solvent evaporation, salting out, spray drying, and supercritical fluid techniques. Choosing the right synthesis method is crucial to

---

[a] *Departamento de Química, Universidad Nacional de Rio Cuarto, Agencia Postal 3, C.P. X5804BYA, Ruta Nacional 36, km 601, Rio Cuarto, Córdoba, Argentina. E-mail: mcorrea@exa.unrc.edu.ar*

[b] *Instituto de Desarrollo Agroindustrial y de la Salud (IDAS), Universidad Nacional de Río Cuarto, Agencia Postal 3, C.P. X5804BYA, Ruta Nacional 36, km 601, Río Cuarto, Córdoba, Argentina*

† Electronic supplementary information (ESI) available. See DOI: https://doi.org/10.1039/d4ra08616c

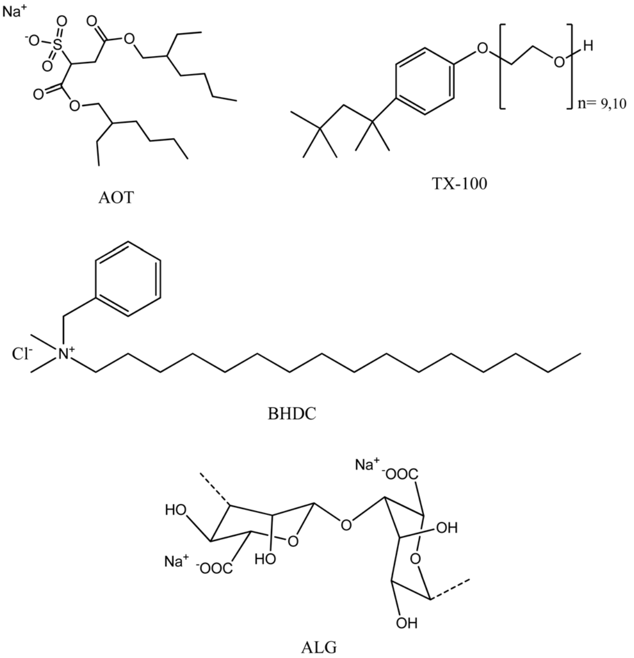

Scheme 1 Chemical structures of AOT, BHDC, TX-100, and sodium alginate.

tailor the properties of the NPs for specific applications, particularly in biomedical and industrial contexts.[12,16,20–22]

Sodium alginate (ALG in Scheme 1) has emerged as a promising biopolymer for nanoparticle synthesis, particularly through ionic gelation, which leverages electrostatic interactions to crosslink polymer chains, leading to the spontaneous formation of ALG-NPs.[23,24] It has been well-documented that metal ions and their complexes are effective in crosslinking linear polymers. In the case of ALG-NPs, divalent ions such as calcium (Ca^{2+}) are commonly used as crosslinkers. However, this approach often results in nanoparticles with inconsistent sizes and morphologies, presenting challenges in achieving precise control over these parameters. This lack of reproducibility limits the broader applicability of the technique in various fields.[23,25–27]

Interestingly, RMs serve as excellent templates for polymeric NP synthesis, offering precise control over the size, shape, and morphology of the resulting NPs.[28] For example, chitosan nanoparticles have been successfully synthesized within *n*-heptane/AOT/water RMs by crosslinking chitosan with glutaraldehyde. The AOT RMs provided a more efficient and straightforward crosslinking environment compared to bulk water.[29]

Building on this approach, we recently developed a method to produce monodisperse and stable ALG-NPs by crosslinking sodium alginate with Ca^{2+} within AOT RMs. By systematically studying the effects of water content, the choice of non-polar solvent, and pH, we identified critical parameters that govern ALG-NP formation. Our results indicate that AOT RMs in *n*-heptane and the biocompatible solvent IPM yield ALG-NPs with sizes strongly influenced by water content. Lower water levels favor tighter interactions between alginate and calcium ions, resulting in smaller NPs, whereas higher water content diminishes crosslinking efficiency.[21] The non-polar solvent choice also plays a pivotal role in nanoparticle size and structure. Compared to *n*-heptane, IPM produces smaller, more tightly crosslinked ALG-NPs at identical water content, likely due to enhanced interfacial interactions that promote cross-linking. Furthermore, increasing the pH of the aqueous phase during resuspension reduces particle size, possibly because higher pH increases the availability of alginate chains for reaction.[21]

This study aims to synthesize ALG-NPs using various RMs as nanotemplates and to explore how the interfaces influence the size and structure of the NPs. To achieve this, we used two probe molecules: *N*,*N*-dimethyl-6-propionyl-2-naphthylamine (PRODAN) and (1*E*,6*E*)-1,7-bis(4-hydroxy-3-methoxyphenyl)-1,6-heptadiene-3,5-dione (curcumin).

PRODAN (Scheme 2) is a widely studied fluorescent probe due to its sensitivity to environmental changes, making it useful in vesicles and RM media. It exhibits significant shifts in absorption and emission spectra as the polarity-polarizability (π^*) and hydrogen donor ability (α) of the medium increase.[30–35] Additionally, PRODAN can be used as a polarity indicator, with the transition energy of its absorption and emission bands correlating well with the polarity parameter $E_{T(30)}$.[35–41]

Curcumin (Scheme 2), a non-toxic natural compound from *Curcuma longa*, has been traditionally used in cooking and medicine. It consists of two methoxylated phenols linked to a β-diketone group (Scheme 2). Curcumin exists in three forms, including two isomers in keto–enol equilibrium and a β-diketone tautomer.[42,43] Numerous studies have highlighted its biological properties, such as antibacterial, antioxidant, anticancer, and anti-inflammatory activities. However, its application is limited by instability, poor bioavailability, and low water solubility due to rapid elimination and poor gastrointestinal absorption.[44–46] Photophysical, photochemical, NMR, and computational studies have explored curcumin's behavior, showing that it adopts the keto–enol form in organic solvents due to intramolecular hydrogen bonds. Early research also revealed that curcumin degrades under light, heat, and pH changes, particularly in neutral or basic conditions, producing degradation products like feruloyl methane, ferulic acid, and vanillin.[42,47–49] To overcome these challenges, recent studies have focused on encapsulation strategies using micelles,

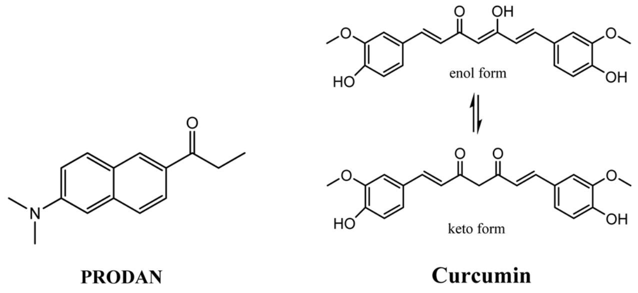

Scheme 2 Molecular structure for PRODAN and curcumin.

vesicles, emulsions, cyclodextrins, and NPs to improve curcumin's solubility, stability, and delivery.[43,46,49–51]

Our work demonstrates that ALG-NPs synthesized using different RMs as nanoreactors exhibit distinct differences in structure and size depending on the type of RM template employed. Specifically, ALG-NPs synthesized within AOT RMs (ALG-NPs@AOT) are the most compact and smallest, with a significantly lower water content within their structure. These findings underscore the critical influence of RM properties on nanoparticle formation and may provide valuable insights into tailoring ALG-NPs for specific applications such as biomedical and industrial fields.

2. Experimental

2.1 Materials

Anhydrous $CaCl_2$ (93% purity) was obtained from Cicarelli®. Sodium alginate with high molecular weight (339.2 kDa), isopropyl myristate (IPM, >98% purity), curcumin, sodium 1,4-bis(2-ethylhexyl) sulfosuccinate, AOT (>99% purity), benzyl-*n*-hexadecyl dimethyl ammonium chloride, BHDC (>99% purity), and poly(oxyethylene) (tetramethylbutyl) phenyl ether, TX-100 were purchased from Sigma-Aldrich®. Surfactants were dried under reduced pressure to constant weight, with no additional purification. The probe molecule 6-propionyl-2-(*N*,*N*-dimethyl) aminonaphthalene (PRODAN) was acquired from molecular probes with 99% purity. All other solvents (cyclohexane, toluene, acetone, and water) were of HPLC grade and obtained from Sintorgan.

2.2 Methods

The ESI† provides detailed procedures for preparing ALG-NPs, AOT, BHDC, and TX-100 RM solutions, and the methodologies for DLS, emission and transmission electron microscopy (TEM) experiments.

3. Results and discussion

The present work aimed to employ RMs as nano templates for achieving uniform and stable ALG-NPs by comparing RMs made by different surfactants. This allows the investigation of the effect of the interface on NP formation.

In prior research,[21] we examined the stability of RMs formed with the anionic surfactant AOT, focusing on interactions involving alginate's negative charge, the presence of Ca^{2+} ions, and the influence of several factors, such as the nonpolar environment and pH. By forming AOT RMs in both *n*-heptane and IPM, we observed that NPs size increased with water content in each solvent. This trend was attributed to variations in crosslinking efficiency, likely influenced by the relative positioning of alginate and calcium ions at lower water concentrations. IPM led to smaller and more crosslinked ALG-NPs compared to *n*-heptane, possibly due to its effect on interfacial interactions. Additionally, increasing the pH of the resuspension medium resulted in smaller NPs, suggesting enhanced alginate availability for cross-linking.

3.1 Effects of different RMs interface on the ALG-NPs production

3.1.1 BHDC RMs. It is well established that BHDC RMs typically form in aromatic rather than hydrocarbon solvents;[7] therefore, toluene was chosen as the nonpolar medium for this investigation.

Table 1 presents the apparent diameter (D_{app}) of the ALG-NPs synthesized using BHDC RMs as nano-templates at various W_0 values, and subsequently resuspended in water at pH 6.5. This highlights the potential of BHDC RMs as effective nanotemplates for ALG-NPs synthesis. The size distribution and stability of the synthesized NPs were analyzed using dynamic light scattering (DLS).

Notably, the results show that ALG-NPs are successfully synthesized using BHDC RMs as nano-templates. Interestingly, when RMs with low water content are employed, the resulting NPs exhibit larger sizes. However, as the W_0 value increases, the NP size decreases, a trend contrary to what is typically expected with larger RMs and different from the findings reported for AOT RMs.[21]

The behavior of Ca^{2+} and ALG within the BHDC RMs depends significantly on the water content (W_0). At low W_0 values, Ca^{2+} ions are located deeper within the polar core, while negatively charged ALG remains close to the cationic interface. This proximity reduces the efficiency of crosslinking, leading to the formation of larger NPs (less crosslinked). Conversely, as the W_0 value increases, ALG migrates to the aqueous core, where it interacts directly with Ca^{2+} ions. This interaction facilitates effective crosslinking, resulting in smaller ALG-NPs.

Importantly, this nanoreactor system enables precise control over the size of the NPs, as increasing the W_0 value consistently reduces the final size of the ALG-NPs. This behavior contrasts sharply with that observed in anionic AOT RMs, where crosslinking is more efficient at low W_0 values, producing smaller NPs under those conditions.[21] Using BHDC/toluene RMs, calcium ions likely migrate to the polar core, accompanied by chloride ions that are displaced from the interface when the polymer (ALG) is incorporated into the micelle.

3.1.2 TX-100 RMs. Two RM systems formed by ionic surfactants have been studied so far, demonstrating the effect of these surfactants on ALG-NP synthesis by varying the water content. Next, the focus shifted to evaluating the role of RMs formed by a non-ionic surfactant in the preparation of ALG-NPs.

As previously mentioned, TX-100 does not form RMs in benzene or *n*-heptane without the presence of a co-surfactant,

Table 1 D_{app} of ALG-NPs obtained by varying the water content (W_0) of the BHDC/toluene RMs and resuspended in water at pH = 6.5. [BHDC] = 0.1 M, [ALG] = 9×10^{-8} M, and [$CaCl_2$] = 9×10^{-4} M. T = 25 °C. In all cases, a single population was observed (100%). PDI = polydispersity index values

W_0	D_{app}(nm)	PDI
5	220 ± 6	0.19 ± 0.01
7	176 ± 4	0.30 ± 0.02
12	112 ± 3	0.35 ± 0.02
15	107 ± 3	0.40 ± 0.02

although exceptions exist when certain solvents, such as cyclohexane, are used.[8] In such case, the water content can reach up to $W_0 = 8$. For the synthesis of ALG-NPs under the methodology applied, the concentrations of the reactants were kept constant ([ALG] = 9×10^{-8} M, [$CaCl_2$] = 9×10^{-4} M, and [TX-100] = 0.7 M), while the W_0 value was systematically varied, and subsequently resuspended in water at pH 6.5.

Table 2 presents the D_{app} values of the ALG-NPs obtained using TX-100 RMs with varying water content.

Firstly, it is evident that ALG-NPs can be synthesized using this micellar system with the designed methodology. The data show that the final diameter of the NPs increases as the W_0 value of the nanoreactor increases, as in the AOT RMs case. Unlike typical ionic surfactants, nonionic surfactants of the poly(oxyethylene) class, such as TX-100, often feature hydrophilic chains that are longer than their hydrophobic counterparts. Consequently, the polar interior of these micelles structurally resembles that of normal micelles in aqueous solution rather than RMs formed by ionic surfactants.[52,53] Additionally, the structure of TX-100 favors the formation of non-spherical RMs.[52,54] Studies on TX-100/cyclohexane RMs have found that the non-polar solvent penetrates the polar core and, upon adding water, it does not form a distinct pool within the polar region but instead disperses among the poly(oxyethylene) chains. As water is added, it gradually displaces the solvent molecules. Given the low solubility of cyclohexane, it is assumed that all the water associates with the surfactant. This displacement of the external solvent by water as W_0 increases leads to an enlargement of the micelle diameter.[8]

Additionally, the addition of reactants to TX-100 RMs also influences its properties. Malik Abdul Rub[55] and collaborators studied the interaction between alginate and TX-100 in aqueous media, proposing that the binding forces include hydrogen bonding, ion-dipole interactions, and van der Waals forces. Alginates reduce the solubility of TX-100 in aqueous systems due to their anionic biopolymer nature, which attracts water through ion-dipole forces. This attraction may decrease the accessibility of water molecules to TX-100, reducing hydrogen bonding and dipole–dipole interactions between the surfactant's –OH groups and the –COOH and –OH groups of alginates.[55] Regarding the addition of $CaCl_2$, studies by D.-M. Zhu and collaborators[8] on TX-100 RM systems showed that adding the salt increases the water solubilization capacity of the micelles while reducing their size. This size reduction is attributed to the formation of complexes or ion-dipole interactions between Ca^{2+} ions and the poly(oxyethylene) chains of the surfactant.

Table 2 D_{app} of ALG-NPs obtained by varying the water content (W_0) of the TX-100/cyclohexane RMs and resuspended in water at pH = 6.5. [TX-100] = 0.7 M, [ALG] = 9×10^{-8} M, and [$CaCl_2$] = 9×10^{-4} M. T = 25 °C. In all cases, a single population was observed (100%). PDI = polydispersity index values

W_0	D_{app} (nm)	PDI
3	149 ± 4	0.35 ± 0.05
5	180 ± 5	0.25 ± 0.04
8	194 ± 5	0.44 ± 0.07

As it was mentioned above several factors can impact the availability of the reactants and size of the nanotemplate in TX-100 RMs. In our case, when the reactants are added to TX-100 RMs, the cross-linking reaction occurs at the interface, and the size of the ALG-NPs depends on the degree of crosslinking between Ca^{2+} and ALG. This cross-linking is more efficient at lower W_0 values as Table 2 shows.

Collectively, these findings highlight the potential of different RMs to effectively control the size of nanomaterials.

It is interesting to present the following discussion on the ALG-NPs sizes compared with the real RMs sizes used as nanotemplates. Table S1† presents the D_{app} of the RMs used as nanoreactors, the sizes of the RMs containing the reactants and, the final size of the ALG-NPs synthesized. As shown, while the ALG-NPs exhibit sizes in the range of 100–200 nm, the different RMs templates have significantly smaller dimensions, around 5–10 nm. Additionally, the presence of nanoparticles inside the RMs does not affect their size. The fact that ALG-NPs exhibit different sizes after extraction from the RMs—despite all samples ultimately being dispersed in bulk water—can be explained by two key factors:

(i) Cross-linking of the ALG NPs: ALG-NPs have strong hydrogen-bonding interactions with water, allowing water incorporation within the nanoparticle matrix, which results in the formation of hydrogel-like structures in bulk water. This swelling phenomenon explains the larger observed sizes of ALG-NPs in aqueous media.[56,57]

(ii) Water properties in RMs: it is well known that the properties of water within RMs differ significantly from those in bulk solution, primarily due to nanoscale confinement and strong interactions with the surfactant interface. These effects have been extensively studied and documented in the literature.[58–60]

These aspects have a profound impact when RMs are used as nanoreactors. As shown in Table S1,† the smaller size of the different RMs used as templates, in which ALG-NPs are initially formed in a non-swollen state, limits their ability to interact with water. After the removal of the RMs, the ALG-NPs transition into their swollen state in bulk water, with their final sizes depending on the efficiency of the crosslinking reaction.

3.1.3 Comparison among the different RM interfaces. The comparison of results from different micellar systems formed by AOT,[21] BHDC, and TX-100 was performed at the same value of $W_0 = 5$ as shown in Table S1,† revealing that the diameters of ALG-NPs vary by a few nanometers across these systems. Notably, the polydispersity indices (PDI) for ALG-NPs prepared in BHDC and TX-100 RMs are slightly higher than those obtained in AOT RMs. However, even in these cases, the size distribution remains narrower compared to ALG-NPs produced through other methods. Moreover, Table S1† shows the zeta potential values for the synthesized ALG-NPs. These results confirm that the ALG-NPs possess a neat negative charge, which is consistent with the charge of alginate in aqueous solution. Furthermore, the zeta potential values indicate that the ALG-NPs are stable. Notably, the ALG-NPs@AOT exhibit a higher zeta potential, suggesting enhanced stability, which prevents their aggregation. These findings are crucial for predicting and controlling the stability and performance of the dispersions, enabling their application in various fields.[61] ALG-NPs synthesized in cationic and nonionic RMs systems exhibit higher PDIs, indicating less monodisperse when compared to those formed in AOT RMs. This difference is closely linked to the distinct interfaces of the micellar systems, which create unique environments for the reaction. The results demonstrate that crosslinking between ALG and Ca^{2+} is effective in all RMs systems studied, but the degree of polydispersity varies. This variation is likely due to differences in the morphology of the RMs, as not all are spherical as the TEM images show in Fig. S2.† The most monodisperse ALG-NPs were prepared in AOT RMs, where the nonpolar solvent plays a crucial role. Its polarity and viscosity allow it to penetrate the micellar interface, shifting calcium ions away from it. The confinement of the anionic polymer, combined with electrostatic repulsions, facilitates the crosslinking reaction between ALG and Ca^{2+}, resulting in more crosslinked and monodisperse particles.

In contrast, in BHDC RMs, the polymer is strongly attracted to the surfactant at low water content, destabilizing the system and leading to larger ALG-NPs. However, as W_0 increases, the polymer becomes more available for crosslinking with calcium, producing smaller NPs.

For nonionic RMs like TX-100, crosslinking is favored at lower water content due to the penetration of the nonpolar solvent into the polar core, along with the addition of $CaCl_2$. In these systems, hydrogen bonding and ion-dipole interactions are significant, enhancing the efficiency of the crosslinking reaction even with less water present.

Overall, these findings underscore the critical role of the RM interface in controlling NP synthesis. Variations in the micellar environment led to differences in particle size, primarily due to the polymer's crosslinking efficiency, which depends on the availability of calcium ions. This highlights the importance of understanding the micellar environment when tailoring the synthesis and properties of nanomaterials.

3.2 The use of ALG-NPs to incorporate different solutes

As discussed above, the final characteristics of the ALG-NPs are strongly dependent on both the amount of water and the nature of the RM interface. Since ALG-NPs are fully biocompatible, we aim to investigate whether the nano-templates used in their synthesis influence their encapsulation capacity, which is expected to depend on the morphology of the NPs.

This section presents results obtained using two different molecules, PRODAN and curcumin (Scheme 2), with a focus on the characterization of ALG-NPs prepared using three different nanoreactor systems: AOT/IPM (denoted as ALG-NPs@AOT),[21] BHDC/toluene (ALG-NPs@BHDC), and TX-100/cyclohexane (ALG-NPs@TX-100). PRODAN was used as a fluorescence probe to investigate the microenvironment and was excited at $\lambda_{exc} = 351$ nm. It is important to note that all studies were performed with ALG-NPs synthesized at $W_0 = 5$ in each of the RM systems.

As previously mentioned, curcumin is highly prone to degradation under certain storage conditions. Therefore, PRODAN, a more stable fluorescent molecule, was chosen for the characterization of the ALG-NPs. PRODAN has been widely used as a probe for micropolarity, and its photophysical properties are particularly useful for characterizing the ALG-NPs synthesized in this study using various micellar interfaces as nanoreactors.[33,36,62,63]

It is important to note that due to the absorption of ALG-NPs in the UV-visible region, the absorption maxima for curcumin and PRODAN were not clearly distinguishable in the spectra. As a result, their encapsulation could not be determined by this technique.

3.2.1 Incorporation of PRODAN and the characterization of the different ALG-NPs. Characterizing ALG-NPs is crucial to understanding the distinct hydrophilic and hydrophobic regions that arise during their formation, a feature that can significantly influence their potential as carriers for bioactive compounds. To better interpret the microenvironment of ALG-NPs in water, the fluorescent probe PRODAN was utilized. In homogeneous media, based on Kamlet and Taft correlations, PRODAN has been shown to effectively sense the micropolarity of its surroundings, exhibiting hypsochromic shifts as micropolarity decreases.[36,64] In the literature, PRODAN has primarily been employed to study membrane structures, lipid–protein interactions, protein–protein interactions, and membrane mimetics such as micelles and vesicles.[31,40,63,65–67] However, there are few reports on PRODAN encapsulation in NPs, and none involving ALG-NPs.[68,69] Due to its high sensitivity to environmental changes, the contributions of different regions within the NPs can be resolved through fluorescence spectrum analysis.[36]

It is important to highlight that none of the emission spectra presented are affected by the emission of the NPs without the probe molecule or by the micelles used as nanotemplates, *i.e.*, in the absence of reactants and probe molecules. Fig. S3 of the ESI† displays these emission spectra. As shown, the small size of both the reverse micelles and the nanoparticles ensures that scattering does not interfere with our spectrophotometric measurements, at least within the wavelength range used in this study.

Fig. 1 shows the emission spectra of PRODAN in the presence of ALG-NPs@AOT resuspended in water. Notable changes are observed by varying the amount of ALG-NPs: in pure water, the emission band is symmetric with a maximum at 525 nm. Upon the initial addition of ALG-NPs@AOT, the intensity of this band decreases while a new band emerges at 420 nm, which increases in intensity as a function of the ALG-NPs. Photophysical studies of PRODAN have reported that this molecule undergoes intramolecular charge transfer (CT) in the excited state following excitation from the ground state.[70] The CT state forms from an initially excited state known as the locally excited (LE) state. In nonpolar environments, emission occurs from the LE state, while in polar environments, it occurs from the CT state.

The emission spectra of PRODAN in the presence of ALG-NPs demonstrate a complex behavior, likely due to the possible heterogeneous structure of the nanoparticles. When interacting with ALG-NPs, PRODAN emits from the CT state in water but transitions to emission from the LE state upon incorporation

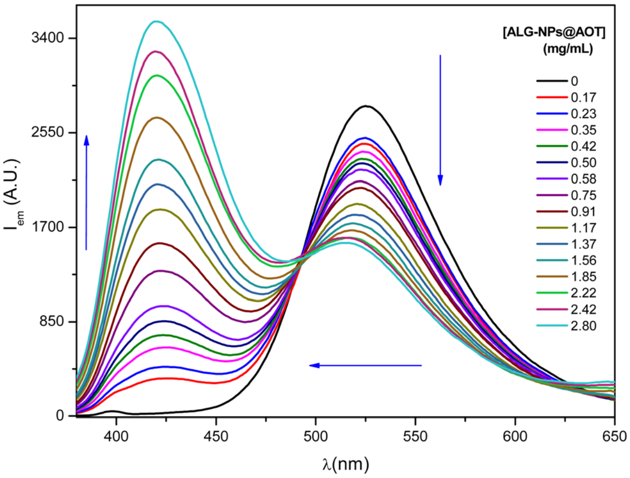

Fig. 1 The emission spectra of PRODAN with varying concentrations of ALG-NPs prepared in AOT RMs at $W_0 = 5$. [PRODAN] = 3×10^{-6} M. $\lambda_{exc} = 351$ nm.

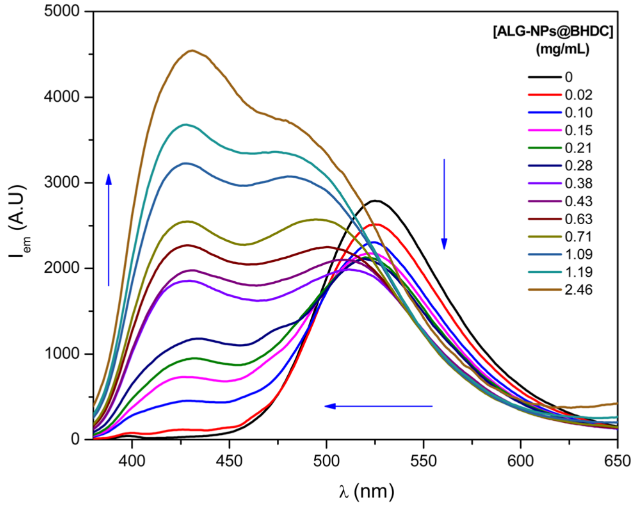

Fig. 2 The emission spectra of PRODAN with varying concentrations of ALG-NPs prepared in BHDC RMs at $W_0 = 5$. [PRODAN] = 3×10^{-6} M, $\lambda_{exc} = 351$ nm.

into the nanoparticles, likely reflecting the low polarity of the encapsulation region. The spectra exhibit a distinct isoemissive point, suggesting that as the concentration of NPs increases, PRODAN partitions into a less polar microenvironment, indicative of its encapsulation within ALG-NPs@AOT. However, at ALG-NPs concentration of 2.8 mg mL^{-1}, complete encapsulation is not achieved, implying that the available NPs are insufficient to incorporate all the PRODAN, leaving a portion of the molecule in the aqueous phase (emitting still at 525 nm).

On the other hand, different results were obtained with the ALG-NPs@BHDC. Fig. 2 presents the fluorescence emission spectra of PRODAN in the presence of ALG-NPs@BHDC in water. Notable changes are observed in the emission band of PRODAN as the concentration of ALG-NPs@BHDC increases. With the initial addition of ALG-NPs@BHDC, the emission band characteristic in pure water begins to decrease in intensity, while a new band emerges at 428 nm.

At lower concentrations of ALG-NPs@BHDC (below 0.28 mg mL^{-1}), an isoemissive point is observed, indicating that PRODAN is partitioning into a less polar microenvironment, signifying its encapsulation. However, when the concentration of ALG-NPs@BHDC reaches 0.38 mg mL^{-1}, the emission band corresponding to pure water begins to deform, undergoing a hypsochromic shift to 477 nm. This shift becomes more pronounced as the concentration of ALG-NPs@BHDC increases, suggesting that PRODAN senses two distinct environments, one less polar than the other.

This behavior suggests that PRODAN is not only encapsulated within the ALG-NPs@BHDC but is also potentially interacting with their surface. In other words, PRODAN appears to sense two distinct microenvironments inside the NPs-ALG@BHDC.

Fig. 3 shows the emission spectra of PRODAN in ALG-NPs prepared with TX-100, ALG-NPs@TX-100. Upon adding a concentration similar to that used for the ALG-NPs prepared with AOT and BHDC, the emission band corresponding to water exhibits a slight blue shift of 6 nm while decreasing in intensity. Additionally, two new bands appear at 415 nm and 439 nm. These results suggest that PRODAN is sensing multiple distinct environments in the NPs. However, no significant increase in the intensity of these bands is observed, suggesting either incomplete encapsulation of PRODAN within these ALG-NPs or a reduction in its quantum yield due to interactions with the nanoparticles. As previously discussed, the polar moiety of TX-100 is highly prone to interacting with encapsulated water molecules. If PRODAN is located in this region, as appears to be the case, hydrogen bonding with interfacial water could be responsible for the observed quenching of its emission.[33,36]

Another possibility is that PRODAN undergoes dual emission within these NPs, emitting simultaneously from both the LE and CT states due to the constrained environment. A similar

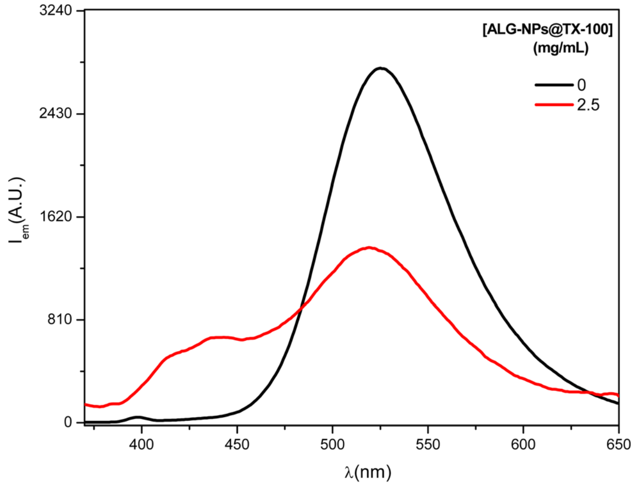

Fig. 3 The emission spectra of PRODAN in pure water and, in ALG-NPs prepared in TX-100 RMs at $W_0 = 5$. [ALG-NPs] = 2.5 mg mL^{-1}, [PRODAN] = 3×10^{-6} M, $\lambda_{exc} = 351$ nm.

phenomenon has been reported for PRODAN dissolved in AOT RMs.[62] To investigate this, we measured the emission lifetime decay of PRODAN at concentrations of NPs around 0.7 mg mL^{-1} and monitored at different emission wavelengths as shown in Table 3. All fitted curves exhibited no negative pre-exponential factors, which are a prerequisite for dual emission.[40]

Table 3 shows the PRODAN emission lifetime values at NPs concentrations of 0.7 mg mL^{-1} and at different emission wavelengths for the BHDC RMs system.

The emission decay of PRODAN in pure water (Table 3) is consistent with previous findings.[33,36,41,62,65] As previously reported, PRODAN exhibits a biexponential decay profile, although the underlying mechanism is not immediately clear. Rowe *et al.*[71] investigated PRODAN in isotropic solvents with varying polarity and hydrogen-bonding properties, proposing that the shorter lifetime corresponds to a solvent-bound locally excited state that undergoes rapid quenching before charge transfer can occur. Our previous work[36] explored the photophysical behavior of PRODAN in water and vesicular environments, suggesting that the shorter lifetime arises from the superposition of two $\pi \rightarrow \pi^*$ transitions primarily localized on the naphthalene ring, with limited charge transfer from the dimethylamine to the carbonyl group in aqueous media. For the ALG-NPs synthesized in different RM templates, the observed emission lifetimes (Table 3) indicate that PRODAN is distributed across distinct microenvironments, a conclusion consistent with prior studies.[36,41] The shortest lifetime is attributed to PRODAN species undergoing quenching due to water exposure[65,72–74] while the longest lifetime corresponds to PRODAN molecules localized in a less polar, water-depleted environment.[41] Notably, the proportion of these distinct PRODAN populations varies depending on the RM system used as a nanotemplate for ALG-NP synthesis. In AOT and BHDC RMs, the percentage of PRODAN species in water is lower than that of PRODAN species located in nonpolar environments. The opposite trend is observed for the TX-100 nanotemplate, where a higher fraction of PRODAN is found in the water-associated environment (Table 3). In the case of BHDC RMs, the emission spectra (Fig. 2) suggest the presence of three distinct PRODAN species residing in different microenvironments, as discussed earlier. Lifetime analysis further supports this interpretation, revealing that at an emission wavelength of 520 nm, the decay follows a triple-exponential model, with the two longer lifetimes corresponding to environments of lower polarity than water.

Table 3 PRODAN fluorescence lifetime (τ, ns) values in water and in ALG-NPs synthesized using different RMs as nanotemplate. [AOT] = 0.1 M [BHDC] = 0.1 M and [TX-100] = 0.70 M [PRODAN] = 3×10^{-6} M; λ_{exc}: 370 nm

	λ_{emi} (nm)	τ_1	%	τ_2	%	τ_3	%	χ^2
PRODAN-water	440	0.65	50.6	2.25	40.4			1.13
ALG-NPs@BHDC	441	0.20	19.5	2.10	80.5			1.06
	520	0.42	19.2	2.3	39.2	4.20	41.6	1.05
ALG-NPs@AOT	440	0.22	17.4	2.8	82.6			1.04
ALG-NPs@TX100	440	0.62	49.2	2.3	50.8			1.03

These findings highlight the structural differences between ALG-NPs synthesized in RMs using different surfactants. The unique micellar interface influences the crosslinking process, resulting in variations in the structure of the resulting ALG-NPs. For example, in the case of ALG-NPs@AOT, PRODAN senses both the polar aqueous environment and a less polar region, but it is located in a single zone within the NPs core. In contrast, in ALG-NPs@BHDC and ALG-NPs@TX-100, PRODAN is distributed across multiple regions, all of which are less polar than water. Additionally, the hydrogen bonding ability of the water in the nonionic system (TX-100) seems to be stronger than in the others.

It appears that the morphology of the NPs plays a key role in PRODAN incorporation. ALG-NPs@AOT exhibit the highest monodispersity. In this system, at low water content, the polymer is confined in a highly restricted environment at the AOT interface, which significantly promotes the crosslinking reaction between ALG and Ca^{2+}. As a result, more crosslinked, monodispersed, and smaller particles are obtained, which are likely to limit PRODAN penetration into different regions of the NPs' core.

On the other hand, in BHDC RMs with low water content, the polymer is strongly attracted to the surfactant. At the same time, the Ca^{2+} ions are repelled due to the interaction with the cationic interface. The crosslinking reaction is less favored, resulting in larger, less compact NPs than ALG-NPs@AOT.

In the case of nonionic TX-100 RMs, crosslinking is less efficient when the aqueous content is low, as water molecules interact with the polar moiety of the surfactant, competing with ALG. This makes it difficult for the Ca^{2+} ions to effectively promote the crosslinking reaction, leading to larger and less compact NPs, similar to those obtained with ALG-NPs@BHDC. The key difference seems to be that the interfacial water in the nonionic RM system is a stronger hydrogen bond donor than the water at the BHDC interface.

Since PRODAN correlates with the $E_{T(30)}$ parameter, it is possible to determine the micropolarity of the environments where it may be located using $E_{T(30)}$ (kcal mol^{-1}) = 147–1.62 × E_{PRODAN}.[36] For ALG-NPs@AOT it was found that at $\lambda_{max,emm}$ = 420 nm, the $E_{T(30)}$ value is 36.7 kcal mol^{-1}, corresponding to the polarity of 1,3-dichlorobenzene and/or thiolate. This indicates that PRODAN is sensing a non-polar microenvironment as suggested.

In ALG-NPs@BHDC, where PRODAN is located in two distinct environments, it was determined that at $\lambda_{max,emi}$ = 428 nm, the $E_{T(30)}$ value is 38.8 kcal mol^{-1}, which corresponds to dimethyl carbonate and/or ethyl chloroacetate. Meanwhile, the band at $\lambda_{max,emi}$ = 477 nm has an $E_{T(30)}$ value of 49.9 kcal mol^{-1}, which corresponds to 2-butoxyethanol. Also, in ALG-NPs@TX-100, where PRODAN senses two distinct environments within the NPs, the less polar environment exhibits a $\lambda_{max,emi}$ = 439 nm, corresponding to an $E_{T(30)}$ value of 41.5 kcal mol^{-1}, which matches the polarity of benzonitrile and/or nitrobenzene. While, the band at $\lambda_{max,emi}$ = 519 nm has an $E_{T(30)}$ value of

57.8 kcal mol^{-1} which corresponds to glycerol and/or formic acid.[36–39]

Thus, it appears that the core of ALG-NPs synthesized in BHDC or TX-100 (which corresponds to the more polar environment observed in BHDC RMs) contains more water and/or more COOH or COO$^-$ free groups because they are less cross-linked. Thus, is likely that these NPs are less rigid compared to those synthesized in AOT.

Additionally, the encapsulation of curcumin within ALG-NPs, excited at $\lambda_{exc} = 423$ nm, is examined.

3.2.2 Incorporation of curcumin in different ALG-NPs. Due to the extent of limitations in using and preserving this very water-insoluble molecule, it is of great interest to investigate the ability of ALG-NPs to protect the molecule and potentially consider them as biocarriers for various applications.

It is known that, depending on the microenvironment of curcumin, it can exhibit excited-state intramolecular hydrogen/proton transfer (ESIHT). Therefore, when curcumin is in water, the molecule exists in the keto–enol form and the intramolecular hydrogen bond typically provides a pathway for rapid non-radiative deactivation in the excited state, resulting in decreased fluorescence intensity.[75]

The emission spectra of curcumin in the different ALG-NPs are shown in Fig. 4. We select a low curcumin concentration (3.5×10^{-5} M) in aqueous solution to assure that it is completely soluble to evaluate the effect of encapsulating in different ALG-NPs. In neat water, the emission maximum of curcumin appears at 555 nm, but these maximum changes depending on the type of ALG-NPs used to encapsulate them. The figure reveals that curcumin encapsulated in ALG-NPs@AOT exhibited a hypsochromic shift with a maximum at 487 nm, along with a significant increase in fluorescence intensity. This suggests the absence of intramolecular hydrogen bonds found in water. Consequently, the quantum yield of curcumin improves as it diffuses from the aqueous medium into a less polar environment, enhancing its solubility and availability.[75,76]

Then, the observed hypsochromic shift may be attributed to the effect of the decrease in polarity and the lack of water to interact through hydrogen bond interaction.[76] This indicates that curcumin is sensing a less polar microenvironment compared to water. Additionally, the emission spectrum shows the presence of shoulders on either side of the emission maximum, one at 464 nm and another at 521 nm. These features could result from curcumin residing in different locations within the ALG-NPs@AOT.

On the other hand, Fig. 4 shows that the emission spectra of curcumin in ALG-NPs@BHDC and ALG-NPs@TX-100 exhibit a broad band with maxima at 554 nm and 549 nm, respectively, showing fluorescence intensities that are not significantly different from curcumin's band in water. This suggests that the encapsulation method may not effectively trap curcumin within these NPs providing little protection and allowing rapid non-radiative deactivation of the compound.

These results are likely due to the different cross-linking experienced by ALG when different surfactants are used in NPs preparation, as well as the variations in NPs size and structural differences of the three ALG-NPs.

Thus, it can be observed that curcumin resides in a low-polarity environment without water molecules when encapsulated in ALG-NPs@AOT, which are more rigid and compact compared to the other NPs. Evidently, those synthesized using BHDC and TX-100 are not suitable for curcumin encapsulation, as their lower cross-linking and greater flexibility allow water molecules to penetrate their interior, which is not ideal for curcumin. This is particularly true for ALG-NPs@TX-100, as demonstrated by PRODAN.

As discussed before, under certain conditions, curcumin becomes unstable and degrades, forming other compounds.[48] To evaluate its stability, fluorescence emission spectra of curcumin in ALG-NPs were recorded after 3 days and shown in Fig. 5. The results showed a decrease in emission intensity for all samples, likely due to the release of the molecule into the

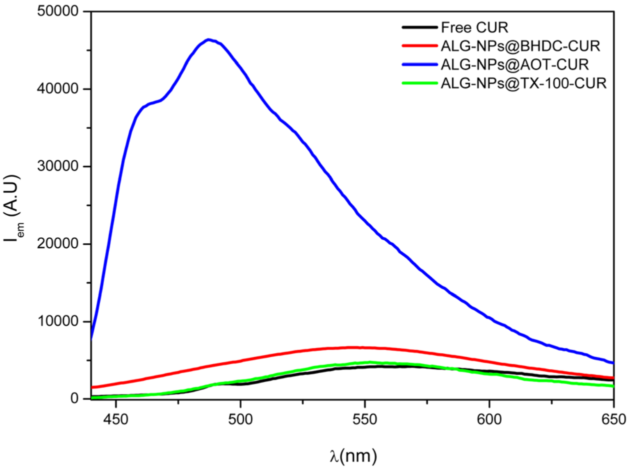

Fig. 4 The emission spectra of curcumin using ALG-NPs synthesized in AOT, BHDC, and TX-100 RMs at $W_0 = 5$. [ALG-NPs] = 1.6 mg mL^{-1}, [curcumin] = 3.5×10^{-5} M, $\lambda_{exc} = 423$ nm.

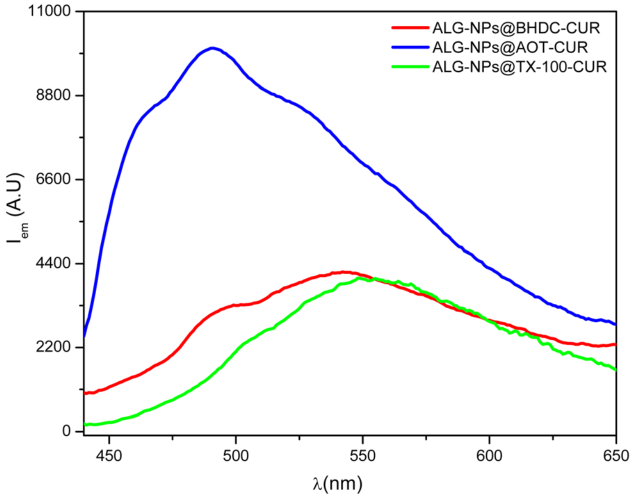

Fig. 5 The emission spectra of curcumin in ALG-NPs synthesized in AOT, BHDC, and TX-100 RMs, after 3 days of visible light exposition.

surrounding medium (water). It is important to note that the samples were stored at $T = 25$ °C and were not protected from visible light. Thus, under these storage conditions, curcumin underwent degradation in different degrees depending on the NPs used.

Notably, curcumin encapsulated in ALG-NPs@AOT did not completely degrade during this time, unlike the curcumin in NPs synthesized in BHDC and TX-100 RMs. These findings suggest that ALG-NPs synthesized in AOT RMs are more effective at protecting curcumin, likely due to the absence of water molecules in their core and/or their ability to degrade first, thus shielding curcumin from degradation.

4. Conclusions

This study demonstrates the significant influence of reverse micelle templates on the structural properties, size, and encapsulation efficiency of ALG-NPs. By systematically varying the interfacial charge and water content within different RMs, we were able to modulate the rigidity, compactness, and water permeability of the resulting ALG-NPs. The nanoparticles synthesized using anionic AOT-based RMs stood out as the most compact and effective carriers for encapsulating curcumin, providing enhanced stability and protection against degradation under ambient conditions.

The versatility of ALG-NPs, combined with their biocompatibility and tunable characteristics, makes them highly promising for a range of applications. Specifically, their potential in food technology to stabilize and deliver sensitive bioactive compounds, such as curcumin, opens new avenues for improving the formulation of functional foods and nutraceuticals. Furthermore, the insights gained in this work about the role of interfacial environments in nanoparticle synthesis may contribute to the development of more efficient encapsulation strategies in biotechnology, pharmaceuticals, and beyond.

The key takeaway from this work is that understanding and controlling interfacial interactions during nanoparticle formation is crucial for developing more advanced, application-specific nanocarriers. Future research could investigate the encapsulation of other sensitive or hydrophobic compounds, further broadening the potential applications of ALG-NPs across diverse scientific and industrial fields.

Data availability

The data supporting the figures and tables in this manuscript were generated using light scattering and emission spectrophotometry equipment and have been included as part of the ESI.†

Author contributions

Fanny Melina Duque: data curation, formal analysis, investigation. R. Dario Falcone: data curation, formal analysis, investigation, writing – review & editing, supervision. N. Mariano Correa: data curation, formal analysis, investigation, writing – original draft, writing – review & editing, supervision, funding acquisition, resources.

Conflicts of interest

There are no conflicts to declare.

Acknowledgements

Financial support from the Consejo Nacional de Investigaciones Científicas y Técnicas, Universidad Nacional de Río Cuarto, and Agencia Nacional de Promoción Científica y Técnica (PICT 2019-0543, PICT 2018-0508, and PICT 2021-112) is gratefully acknowledged. R. D. F. and N. M. C. hold a research position at the CONICET. F. M. D. thanks CONICET for a doctoral fellowship.

References

1 M. L. de Moraes and L. Caseli, Supramolecular systems, in *Nanostructures*, Elsevier, 2017, pp. 33–52.

2 M. Bourrel and R. S. Schechter, *Microemulsions and Related Systems: Formulation, Solvency, and Physical*, Technips, 2010.

3 M.-L. Arsene, *et al.*, Versatility of reverse micelles: from biomimetic models to nano (Bio)sensor design, *Processes*, 2021, **9**, 345.

4 M. S. Z. Shiri, W. Henderson, A. M. Henning and M. R. Mucalo, Synthesis study of size-controlled rhenium nanoparticle systems using reverse micelle-based methodologies, *Colloids Surf., A*, 2024, **694**, 134150.

5 S. Ghosh, A. Ray and N. Pramanik, Self-assembly of surfactants: an overview on general aspects of amphiphiles, *Biophys. Chem.*, 2020, **265**, 106429.

6 V. R. Girardi, J. J. Silber, N. Mariano Correa and R. Darío Falcone, The use of two non-toxic lipophilic oils to generate environmentally friendly anionic reverse micelles without cosurfactant. Comparison with the behavior found for traditional organic non-polar solvents, *Colloids Surf., A*, 2014, **457**, 354–362.

7 F. M. Agazzi, R. D. Falcone, J. J. Silber and N. M. Correa, Solvent blends can control cationic reversed micellar interdroplet interactions. The effect of n- heptane : Benzene mixture on BHDC reversed micellar interfacial properties: droplet sizes and micropolarity, *J. Phys. Chem. B*, 2011, **115**, 12076–12084.

8 D. M. Zhu, K. I. Feng and Z. A. Schelly, Reverse micelles of triton X-100 in cyclohexane. Effects of temperature, water content, and salinity on the aggregation behavior, *J. Phys. Chem.*, 1992, **96**, 2382–2385.

9 P. Thadapaneni and J. C. Deák, Investigation of the shapes and sizes of soft molecular aggregates in solution *via* partial molar volume and dynamic light scattering measurements, *J. Mol. Liq.*, 2024, **396**, 123947.

10 N. M. Correa, J. J. Silber, R. E. Riter and N. E. Levinger, Nonaqueous polar solvents in reverse micelle systems, *Chem. Rev.*, 2012, **112**, 4569–4602.

11 S. Malik, K. Muhammad and Y. Waheed, Nanotechnology: a revolution in modern industry, *Molecules*, 2023, **28**, 661.

12 A. Aziz Shaikh, *et al.*, Biopolymer-based nanocomposites for application in biomedicine: a review, *J. Polym. Eng.*, 2024, **44**, 83–116.

13 S. Khizar, *et al.*, Nanocarriers based novel and effective drug delivery system, *Int. J. Pharm.*, 2023, **632**, 122570.

14 D. Gaikwad, R. Sutar and D. Patil, Polysaccharide mediated nanodrug delivery: a review, *Int. J. Biol. Macromol.*, 2024, **261**, 129547.

15 P. Garbati, *et al.*, Targeting the gut: a systematic review of specific drug nanocarriers, *Pharmaceutics*, 2024, **16**, 431.

16 J. Zhang, P. Zhan and H. Tian, Recent updates in the polysaccharides-based Nano-biocarriers for drugs delivery and its application in diseases treatment: a review, *Int. J. Biol. Macromol.*, 2021, **182**, 115–128.

17 A. Altaf, Z. Usmani, A. H. Dar and K. K. Dash, A comprehensive review of polysaccharide-based bionanocomposites for food packaging applications, *Discover Food*, 2022, **2**, 10.

18 M. Soni, *et al.*, Nanoencapsulation strategies for improving nutritional functionality, safety and delivery of plant-based foods: recent updates and future opportunities, *Plant Nano Biology*, 2022, **1**, 100004.

19 M. Jiang and Y. Zhang, Biopolymer-based encapsulation of anthocyanins as reinforced natural colorants for food applications, *J. Agric. Food Res.*, 2023, **11**, 100488.

20 Y. Fan, *et al.*, Natural polysaccharides based self-assembled nanoparticles for biomedical applications – A review, *Int. J. Biol. Macromol.*, 2021, **192**, 1240–1255.

21 F. M. Duque, N. Mariano Correa and R. Dario Falcone, Alginate nanoparticle synthesis using n-heptane and isopropyl myristate/AOT reverse micelles: the impact of the non-polar solvent, water content, and pH on the particle size and cross-linking efficiency, *New J. Chem.*, 2024, **48**, 16169–16176.

22 S. Ahadian, *et al.*, Micro and nanoscale technologies in oral drug delivery, *Adv. Drug Deliv. Rev.*, 2020, **157**, 37–62.

23 J. P. Paques, E. Van Der Linden, C. J. M. Van Rijn and L. M. C. Sagis, Preparation methods of alginate nanoparticles, *Adv. Colloid Interface Sci.*, 2014, **209**, 163–171.

24 J. P. Paques, Alginate nanospheres prepared by internal or external gelation with nanoparticles, in *Microencapsulation and Microspheres for Food Applications*, Elsevier Inc., 2015, pp. 39–55.

25 A. Froelich, *et al.*, Alginate-based materials loaded with nanoparticles in wound healing, *Pharmaceutics*, 2023, **15**, 1142.

26 A. Saxena, *et al.*, Synthesis of alginate nanogels with polyvalent 3D transition metal cations: applications in urease immobilization, *Polymers*, 2022, **14**, 1277.

27 I. P. S. Fernando, W. Lee, E. J. Han and G. Ahn, Alginate-based nanomaterials: fabrication techniques, properties, and applications, *Chem. Eng. J.*, 2019, **391**, 123823.

28 F. M. Duque, N. M. Correa and R. D. Falcone, Reverse micelles: a versatile platform for the generation of highly controlled polymeric nanoparticles, in *Advances in Physical Organic Chemistry*, Academic Press Inc., 2024, pp. 39–59.

29 M. S. Orellano, C. Porporatto, J. J. Silber, R. D. Falcone and N. M. Correa, AOT reverse micelles as versatile reaction media for chitosan nanoparticles synthesis, *Carbohydr. Polym.*, 2017, **171**, 85–93.

30 G. Weber and F. J. Farris, Synthesis and spectral properties of a hydrophobic fluorescent probe: 6-propionyl-2-(dimethylamino)naphthalene, *Biochemistry*, 1979, **18**, 3075–3078.

31 N. Kanwa, A. Patnaik, S. K. De, M. Ahamed and A. Chakraborty, Effect of surface ligand and temperature on lipid vesicle-gold nanoparticle interaction: a spectroscopic investigation, *Langmuir*, 2019, **35**, 1008–1020.

32 O. M. Zharkova and Y. P. Morozova, Use of fluorescent probes to estimate solvent polarity, *Russ. Phys. J.*, 2013, **56**, 257–263.

33 M. Novaira, M. A. Biasutti, J. J. Silber and N. M. Correa, New insights on the photophysical behavior of PRODAN in anionic and cationic reverse micelles: from which state or states does it emit?, *J. Phys. Chem. B*, 2007, **111**, 748–759.

34 N. Ito, N. M. Watanabe, Y. Okamoto and H. Umakoshi, Multiplicity of solvent environments in lipid bilayer revealed by DAS deconvolution of twin probes: comparative method of Laurdan and Prodan, *Biophys. J.*, 2023, **122**, 4614–4623.

35 B. Sengupta, J. Guharay and P. K. Sengupta, Characterization of the fluorescence emission properties of prodan in different reverse micellar environments, *Spectrochim. Acta, Part A*, 2000, **56**, 1433–1441.

36 F. Moyano, M. A. Biasutti, J. J. Silber and N. M. Correa, New insights on the behavior of PRODAN in homogeneous media and in large unilamellar vesicles, *J. Phys. Chem. B*, 2006, **110**, 11838–11846.

37 C. Reichardt and T. Welton, *Solvents and Solvent Effects in Organic Chemistry*, Wiley, Weinheim, 2010.

38 Y. Marcus, The properties of organic liquids that are relevant to their use as solvating solvents, *Chem. Soc. Rev.*, 1993, **22**, 409–416.

39 J. M. Abboud, *et al.*, Critical compilation of scales of solvent parameters. Part I. Pure, non hydrogen bond donor solvents (Technical Report), *Pure Appl. Chem.*, 1999, **71**, 645–718.

40 F. M. Agazzi, J. Rodriguez, R. D. Falcone, J. J. Silber and N. M. Correa, PRODAN dual emission feature to monitor BHDC interfacial properties changes with the external organic solvent composition, *Langmuir*, 2013, **29**, 3556–3566.

41 M. A. Luna, *et al.*, PRODAN photophysics as a tool to determine the bilayer properties of different unilamellar vesicles composed of phospholipids, *Langmuir*, 2024, **40**, 657–667.

42 F. Payton, P. Sandusky and W. L. Alworth, NMR study of the solution structure of curcumin, *J. Nat. Prod.*, 2007, **70**, 143–146.

43 Deepshikha, A. Kumar, K. Shalu and D. Narula, Recent advances of rhamnolipids nanocarriers for the delivery of

bioactive curcumin: a review, *Mater. Today Proc.*, 2023, DOI: **10.1016/j.matpr.2023.03.813**.

44 S. Divyashree, J. Sharath, P. Janhavi, S. Deepashree and S. P. Muthukumar, Curcumin and its derivatives as nutraceuticals: an update, in *Studies in Natural Products Chemistry*, Elservier, 2023, vol. 77, pp. 135–162.

45 A. Singh, S. Dasgupta, A. Bhattacharya, G. Mukherjee and K. Chaudhury, Therapeutic potential of curcumin in endometrial disorders: current status and future perspectives, *Drug Discovery Today*, 2022, **27**, 900–911.

46 K. Gayathri, M. Bhaskaran, C. Selvam and R. Thilagavathi, Nano formulation approaches for curcumin delivery-a review, *J. Drug Deliv. Sci. Technol.*, 2023, **82**, 104326.

47 S. Mondal, S. Ghosh and S. P. Moulik, Stability of curcumin in different solvent and solution media: UV-visible and steady-state fluorescence spectral study, *J. Photochem. Photobiol. B*, 2016, **158**, 212–218.

48 K. I. Priyadarsini, Photophysics, photochemistry and photobiology of curcumin: studies from organic solutions, bio-mimetics and living cells, *J. Photochem. Photobiol. C: Photochem. Rev.*, 2009, **10**, 81–95.

49 M. Rezaeisadat, A. K. Bordbar and R. Omidyan, Molecular dynamics simulation study of curcumin interaction with nano-micelle of PNIPAAm-b-PEG co-polymer as a smart efficient drug delivery system, *J. Mol. Liq.*, 2021, **332**, 115862.

50 Y. Hu, *et al.*, Encapsulation, protection, and delivery of curcumin using succinylated-cyclodextrin systems with strong resistance to environmental and physiological stimuli, *Food Chem.*, 2022, **376**, 131869.

51 A. F. Cañon-Ibarra, L. T. Sanchez, A. Rosales Rivera, D. Blach and C. C. Villa, Curcumin capped magnetic nanoparticles. Synthesis, characterization and photoinactivation activity against *S. Aureus*, *Results Chem.*, 2023, **5**, 4–9.

52 Z. Wu, *et al.*, Solid and hollow nanoparticles template using non-ionic surfactant-based reverse micelles and vesicles, *Colloids Surf., A*, 2022, **634**, 127917.

53 L. Abu-Ghunmi, M. Badawi and M. Fayyad, Fate of triton X-100 applications on water and soil environments: a review, *J. Surfactants Deterg.*, 2014, **17**, 833–838.

54 Y. Zhang, B. Zhen, Y. Hu, G. Liang and Y. Feng, A reverse micellar system with Triton X-100: effect of surfactant polydispersity and preparation of monodisperse silica nanoparticles, *Soft Matter*, 2020, **16**, 383–389.

55 M. Abdul Rub, M. Anamul Hoque, N. Azum and S. Mahbub, Investigation of the aggregation, clouding and thermodynamics of the mixture of sodium alginate with sodium dodecyl sulfate and triton X-100 in aqueous and aqua-organic mixed solvents media, *J. Mol. Liq.*, 2022, **346**, 117109.

56 J. Tan, *et al.*, Development of alginate-based hydrogels: crosslinking strategies and biomedical applications, *Int. J. Biol. Macromol.*, 2023, **239**, 124275.

57 N. Nezamdoost-Sani, M. A. Khaledabad, S. Amiri and A. Mousavi Khaneghah, Alginate and derivatives hydrogels in encapsulation of probiotic bacteria: an updated review, *Food Biosci.*, 2023, **52**, 102433.

58 N. M. Correa and N. E. Levinger, What can you learn fom a molecular probe? New insights on the behavior of C343 in homogeneous solutions and AOT reverse micelles, *J. Phys. Chem. B*, 2006, **110**, 13050–13061.

59 H. S. Tan, I. R. Piletic and M. D. Fayer, Orientational dynamics of water confined on a nanometer length scale in reverse micelles, *J. Chem. Phys.*, 2005, **122**, 174501.

60 D. Cringus, *et al.*, Ultrafast energy transfer in water – AOT reverse micelles, *J. Phys. Chem. B*, 2007, **111**, 14193–14207.

61 A. Serrano-Lotina, *et al.*, Zeta potential as a tool for functional materials development, *Catal. Today*, 2023, **423**, 113862.

62 M. Novaira, *et al.*, An example of how to use AOT reverse micelle interfaces to control a photoinduced intramolecular charge-transfer process, *Langmuir*, 2008, **24**, 4637–4646.

63 A. González Herrera, N. Mariano Correa, R. Dario Falcone and F. Moyano, Unveiling eco-friendly reverse micelle systems: dimethyl carbonate as a novel biocompatible solvent, *ChemPhysChem*, 2024, **25**, e202400617.

64 M. J. Kamlet, J. L. Abboud and R. W. Taft, The solvatochromic comparison method. 6. The π* scale of solvent polarities, *J. Am. Chem. Soc.*, 1977, **99**, 6027–6038.

65 M. S. Orellano, D. A. Chiappetta, J. J. Silber, R. D. Falcone and N. M. Correa, Monitoring the microenvironment inside polymeric micelles using the fluorescence probe 6-propionyl-2-dimethylaminonaphthalene (PRODAN), *J. Mol. Liq.*, 2021, **343**, 117552.

66 M. Oliver, A. Bauzá, A. Frontera and M. Miró, Fluorescent lipid nanoparticles as biomembrane models for exploring emerging contaminant bioavailability supported by density functional theory calculations, *Environ. Sci. Technol.*, 2016, **50**, 7135–7143.

67 N. Kanwa, S. K. De, C. Adhikari and A. Chakraborty, Spectroscopic study of the interaction of carboxyl-modified gold nanoparticles with liposomes of different chain lengths and controlled drug release by layer-by-layer technology, *J. Phys. Chem. B*, 2017, **121**, 11333–11343.

68 F. Palomba, *et al.*, Mapping heterogeneous polarity in multicompartment nanoparticles, *Sci. Rep.*, 2018, **8**, 1–8.

69 F. B. Landry, D. V. Bazile, G. Spenlehauer, M. Veillard and J. Kreuter, Release of the fluorescent marker Prodan® from poly(D,L-lactic acid) nanoparticles coated with albumin or polyvinyl alcohol in model digestive fluids (USP XXII), *J. Control. Release*, 1997, **44**, 227–236.

70 A. M. Rollinson and H. G. Drickamer, High pressure study of luminescence from intramolecular CT compounds, *J. Chem. Phys.*, 1980, **73**, 5981–5996.

71 B. A. Rowe, *et al.*, Spectral heterogeneity of PRODAN fluorescence in isotropic solvents revealed by multivariate photokinetic analysis, *J. Phys. Chem. A*, 2008, **112**, 13402–13412.

72 Y. Y. Nikitina, E. S. Iqbal, H. J. Yoon and C. J. Abelt, Preferential solvation in carbonyl-twisted PRODAN derivatives, *J. Phys. Chem. A*, 2013, **117**, 9189–9195.

73 I. G. Alty, *et al.*, Intramolecular hydrogen-bonding effects on the fluorescence of PRODAN derivatives, *J. Phys. Chem. A*, 2016, **120**, 3518–3523.

74 O. Golfetto, E. Hinde and E. Gratton, Laurdan fluorescence lifetime discriminates cholesterol content from changes in fluidity in living cell membranes, *Biophys. J.*, 2013, **104**, 1238–1247.

75 S. Mohanty, B. Tirkey, S. R. Jena, L. Samanta and U. Subuddhi, Exploring steroidal surfactants as potential drug carriers for an anticancer drug curcumin: an insight into the effect of surfactants' structure on the photophysical properties, stability, and activity of curcumin, *Langmuir*, 2023, **39**, 1852–1869.

76 S. M. Khopde, K. Indira Priyadarsini, D. K. Palit and T. Mukherjee, Effect of solvent on the excited-state photophysical properties of curcumin, *Photochem. Photobiol.*, 2007, **72**, 625–631.